JOURNAL OF SOLID STATE CHEMISTRY

Volume 179, Number 1, January 2006

CONTENTS

Selected-control solution-phase route to multiple-dendritic and cuboidal structures of PbSe

Benxia Li, Yi Xie, Yang Xu, Changzheng Wu and Zhengquan Li

Page 56

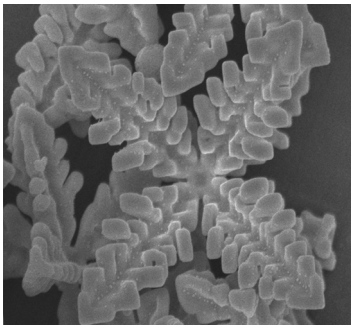

PbSe multiple-dendritic hierarchical structure with 4-fold structural symmetry and cuboidal microcrystals with concave faces were selectively obtained by using different selenium sources in a glycerol/water solution system.

Visible-light-driven photocatalyst of Bi_2WO_6 nanoparticles prepared via amorphous complex precursor and photocatalytic properties

Shicheng Zhang, Chuan Zhang, Yi Man and Yongfa Zhu

Page 62

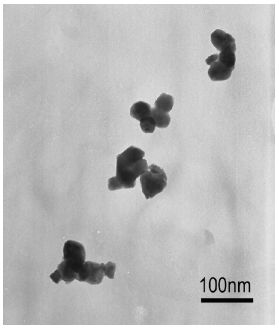

Bi_2WO_6 nanoparticles obtained from amorphous complex precursor under 450 °C for 24 h.

Structure and magnetism of 4H-$BaMnO_{3-x}$ ($0 \leqslant x \leqslant 0.35$) and 4H-$Ba_{0.5}Sr_{0.5}MnO_{3-x}$ ($0 \leqslant x \leqslant 0.21$)

Josephine J. Adkin and Michael A. Hayward

Page 70

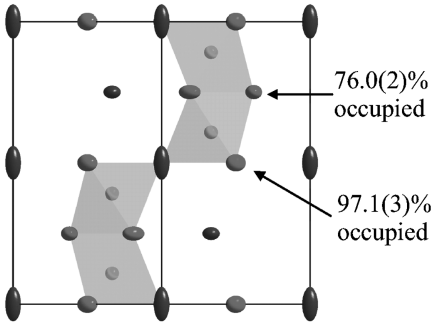

Anion vacancy locations in 4H-$BaMnO_{3-x}$.

Heat capacity, enthalpy and entropy of bismuth niobate and bismuth tantalate

M. Hampl, A. Strejc, D. Sedmidubský, K. Růžička, J. Hejtmánek and J. Leitner

Page 77

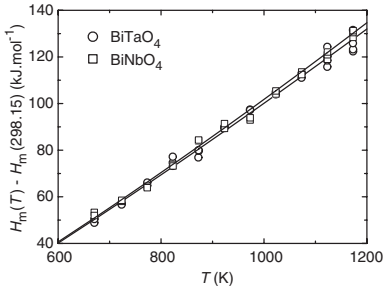

Heat content of bismuth niobate and bismuth tantalate—experimental points determined by the drop method and temperature dependencies obtained by the simultaneous fit of heat capacity and heat content data.

Magnetic structures of the α-$Li_3Fe_2(PO_4)_{3-x}(AsO_4)_x$ ($x = 1, 1.5, 2, 3$) solid solution

Aintzane Goñi, José Luis Mesa, José Luis Pizarro, Leopold Fournés, Alain Wattiaux, Roger Olazcuaga, María Isabel Arriortua and Teófilo Rojo

Page 81

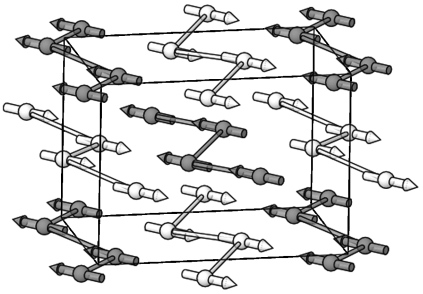

The solid solution exhibits two ferromagnetic sublattices antiferromagnetically coupled due to the existence of two crystallographically independent iron sites, which are affected by the arsenate-phosphate substitution.

Synthesis of nickel nanoparticles and carbon encapsulated nickel nanoparticles supported on carbon nanotubes

Jipeng Cheng, Xiaobin Zhang and Ying Ye

Page 91

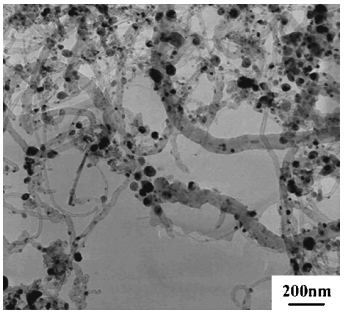

TEM image of nickel nanoparticles supported on carbon nanotubes.

Continued

Sacrificial template growth of CdS nanotubes from $Cd(OH)_2$ nanowires
Xuemei Li, Haibin Chu and Yan Li
Page 96

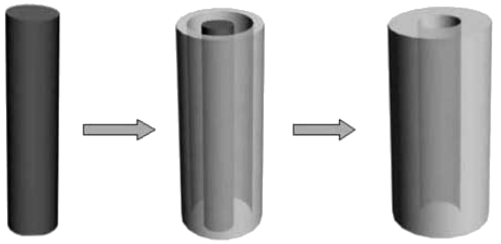

CdS nanotubes were prepared with $Cd(OH)_2$ nanowires as the sacrificial templates. Diffusion played an important role in the process. The morphology of the produced nanotubes can be varied by alternating the reaction conditions.

Crystal structure and vibrational properies of $Rb_2MgWO_2(PO_4)_2$—A new framework phosphate
M. Mączka, A. Waśkowska and J. Hanuza
Page 103

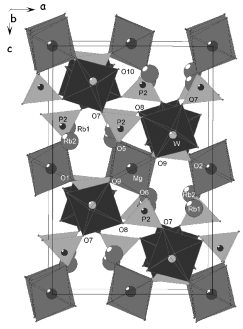

Projection of the $Rb_2MgWO_2(PO_4)_2$ crystal structure along the *b*-axis.

Electron-doping through La^{III}-for-Sr^{II} substitution in $(Sr_{1-x}La_x)_2FeTaO_6$: Effects on the valences and ordering of the *B*-site cations, Fe and Ta
E.-L. Rautama, T.S. Chan, R.S. Liu, J.M. Chen, H. Yamauchi and M. Karppinen
Page 111

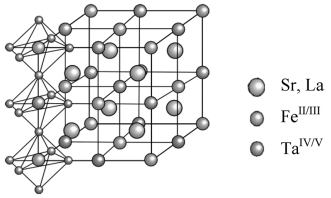

Valence states of Fe and Ta are controlled in the partially ordered perovskite oxide, $(Sr,La)_2FeTaO_6$, through aliovalent La^{III}-for-Sr^{II} substitution.

Dynamics of superionic $Rb_3H(SeO_4)_2$ single crystals studied by ^1H and ^{87}Rb spin–lattice relaxation
Ae Ran Lim and M. Ichikawa
Page 117

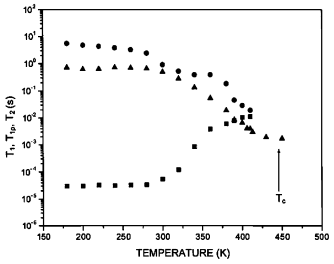

Temperature dependencies of the spin–lattice relaxation time in the laboratory frame, T_1, spin–lattice relaxation time in the rotating frame, $T_{1\rho}$, and spin–spin relaxation time, T_2, for ^1H in a $Rb_3H(SeO_4)_2$ single crystal ((●) T_1, (▲) $T_{1\rho}$, and (■) T_2).

Hydrothermal synthesis and characterization of two new bicapped Keggin heteropoly tungstovanadated derivatives
Ya-Bing Liu, Li-Mei Duan, Xiao-Mei Yang, Ji-Qing Xu, Qing-Bin Zhang, Yu-Kun Lu and Jian Liu
Page 122

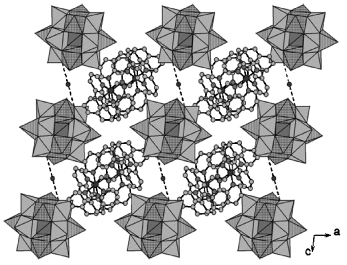

Two new heteropoly tungstovanadate derivatives, $[Fe(phen)_3]_2[W_{10.5}V_{4.5}O_{42}]\cdot 3H_2O$(**1**) and $[Fe(phen)_3]_2[W_{10}V_5O_{42}]\cdot 6H_2O$(**2**) (phen = 1,10′-phenanthroline), have been synthesis under hydrothermal conditions by using different starting materials. Compound **1** is the first example of discrete bicapped Keggin heteropoly tungstovanadates. Polyoxoanions, $[Fe(phen)_3]^{2+}$ cations and water molecules act as building blocks to form two-dimensional (2-D) supramolecular layers through extensive hydrogen bonding.

Synthesis and structure of the ternary and quaternary strontium nitride halides, $Sr_2N(X, X')$ (X, X' = Cl, Br, I)
Amy Bowman, Ronald I. Smith and Duncan H. Gregory
Page 130

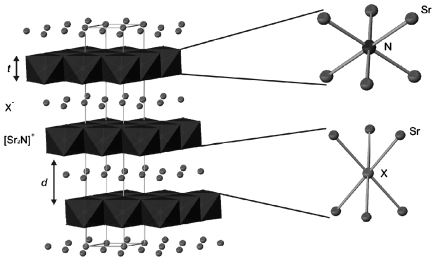

New ternary and quaternary nitride halides, Sr_2N(Cl, Br) and Sr_2N(Br, I) have been synthesised. The HCP layered structures of the insulating nitride halides persist irrespective of the halide, X, or the temperatures investigated.

Ferromagnetic-phase transition in the spinel-type $CuCr_2Te_4$
Takeshi Suzuyama, Junji Awaka, Hiroki Yamamoto, Shuji Ebisu, Masakazu Ito, Takashi Suzuki, Takao Nakama, Katsuma Yagasaki and Shoichi Nagata
Page 140

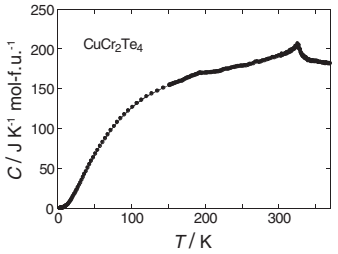

Molar heat capacity of $CuCr_2Te_4$ over a wide temperature range of 2.17–373 K.

Inorganic–organic hybrid compounds: Synthesis and characterization of three new metal phosphonates with similar characteristic structural features
Sebastian Bauer, Thomas Bein and Norbert Stock
Page 145

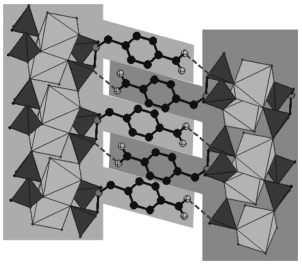

Hydrothermal reactions of the phosphonocarboxylic acid $H(HO_3PCH_2)_2NH\text{-}CH_2C_6H_4\text{-}COOH$ with Sm^{3+} and Ca^{2+} salts has led to three new inorganic–organic hybrid compounds. All crystal structures contain phosphonate zwitterions and have a layer-like arrangement. The rigid organic groups arrange in a "zipper-like" fashion and hydrogen bonding plays an important role in the stabilization of the crystal structures.

Hydrothermal synthesis and characterization of a new three-dimensional hybrid zinc phosphate $[Zn_2(HPO_4)_2(4,4'\text{-bipy})]\cdot 3H_2O$ with neutral porous framework
Lei Wang, Ming Yang, Guanghua Li, Zhan Shi and Shouhua Feng
Page 156

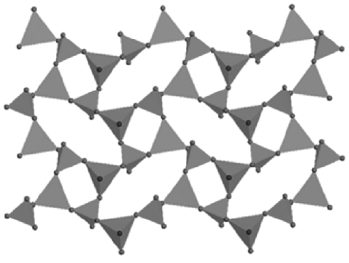

View of the two-dimensional neutral zinc phosphate layer along the *bc* plane.

Magnetic and vibrational properties and crystal structure of $Sr_{9.2}Co_{1.3}(PO_4)_7$ with disordered arrangements of some strontium, cobalt, and phosphate ions
Alexei A. Belik, Artem P. Malakho, Petro S. Salamakha and Bogdan I. Lazoryak
Page 161

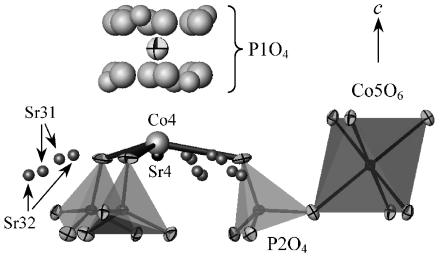

Disordered structural elements in $Sr_{9.2}Co_{1.3}(PO_4)_7$: the $P1O_4$ tetrahedron and the Sr31, Sr32, Sr4, and Co4 sites. The Co4—O22 bonds and ordered $P2O_4$ and $Co5O_6$ polyhedra are also shown.

High-pressure synthesis and crystal structure analysis of $NaMn_2O_4$ with the calcium ferrite-type structure
Junji Akimoto, Junji Awaka, Norihito Kijima, Yasuhiko Takahashi, Yuichi Maruta, Kazuyasu Tokiwa and Tsuneo Watanabe
Page 169

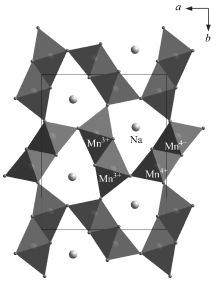

Crystal structure of $NaMn_2O_4$ viewed along [001]. The manganese valence Mn^{3+}/Mn^{4+} ordering has been observed in the two "double rutile" chains in $NaMn_2O_4$.

Syntheses and crystal structures of a series of new divalent metal phosphonates with imino-bis(methylphosphonic acid)
Bing-Ping Yang, Andrey V. Prosvirin, Han-Hua Zhao and Jiang-Gao Mao
Page 175

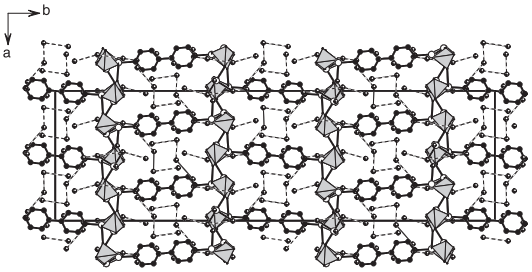

View of the pillar-layered structure of **4** down the *c*-axis. The C–PO_3 tetrahedra are graded in light gray. Cu, N and O atoms are represented by open, octand and crossed circles, respectively. Hydrogen bonds are represented by dashed lines.

Continued

Crystal structures of alkali-metal indium (III) phosphates of $[M_3In(PO_4)_2]_n$ (M = K, $n = 10$; M = Rb, $n = 2$) compounds, and band structures and chemical bond properties of $[Rb_3In(PO_4)_2]_2$ crystal

Yongchun Zhang, Wendan Cheng, Dongsheng Wu, Hao Zhang, Dagui Chen, Yajing Gong, Zigui Kan and Jing Zhu

Page 186

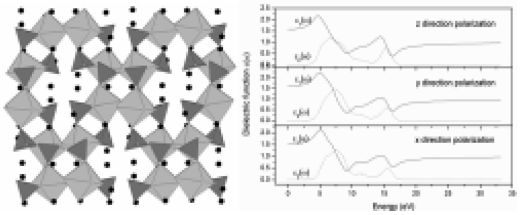

Crystal structure and dielectric functions of $[Rb_3In(PO_4)_2]_2$.

Structure and magnetism of $NaRu_2O_4$ and $Na_{2.7}Ru_4O_9$

K.A. Regan, Q. Huang, M. Lee, A.P. Ramirez and R.J. Cava

Page 195

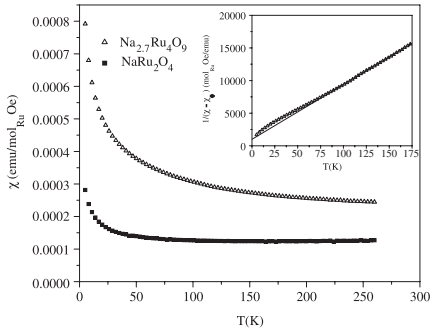

Magnetic susceptibility vs. temperature data for $NaRu_2O_4$ (■) and $Na_{2.7}Ru_4O_9$ (△). $\chi_0 = 1.2 \times 10^{-4}$ emu/mol$_{Ru}$ Oe for $NaRu_2O_4$, $\chi_0 = 2.0 \times 10^{-4}$ emu/mol$_{Ru}$ Oe for $Na_{2.7}Ru_4O_9$. Inset: Inverse magnetic susceptibility vs. temperature data for $Na_{2.7}Ru_4O_9$. A linear fit of the high temperature data from 125 to 200 K shows Curie–Weiss behavior, giving $\Theta_{cw} = -11.8$ K and $C = 0.0119$ emu/mol Oe K.

The actual structure of $K_6(VO)_2(V_2O_3)_2(PO_4)_4(P_2O_7)$: Ordered distribution of P_2O_7 groups and charge ordering of vanadium

A. Leclaire and B. Raveau

Page 205

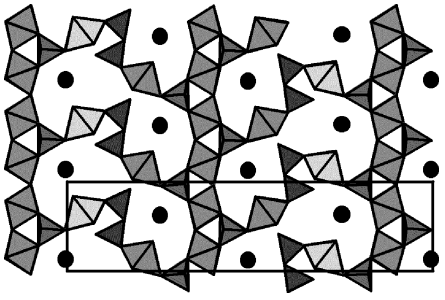

Partial projection showing the ordering of the P_2O_7 units (in dark gray) and the ordering of the V^{5+} (light gray) and of the V^{4+} (medium gray) species.

Effect of La filling on thermoelectric properties of $La_xCo_{3.6}Ni_{0.4}Sb_{12}$-filled skutterudite prepared by MA–HP method

Junyou Yang, Yuehua Chen, Wen Zhu, Jiangying Peng, Siqian Bao, Xi'an Fan and Xingkai Duan

Page 212

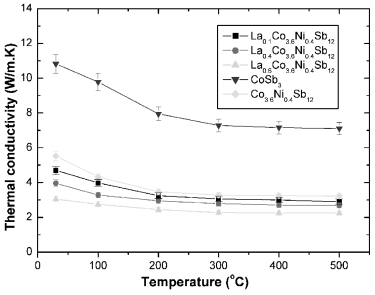

Thermal conductivity of the filled skutterudite versus temperature and La filling content.

Synthesis and properties of pyrazine-pillared $Ag_3Mo_2O_4F_7$ and $AgReO_4$ layered phases

Haisheng Lin, Bangbo Yan, Paul D. Boyle and Paul A. Maggard

Page 217

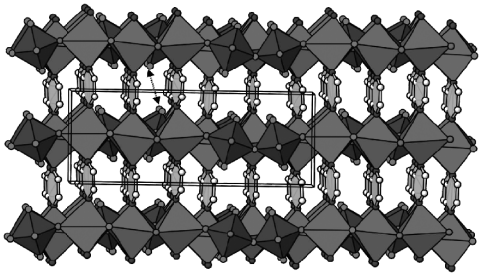

An ~[010] edge-on view of the pyrazine-bridged layers in $Ag_3Mo_2O_4F_7(pyz)_3$. Both the unit cell and the shortest interlayer F–F distance are marked.

Preparation of monodispersed microporous SiO_2 microspheres with high specific surface area using dodecylamine as a hydrolysis catalyst

Jiaguo Yu, Li Zhao and Bei Cheng

Page 226

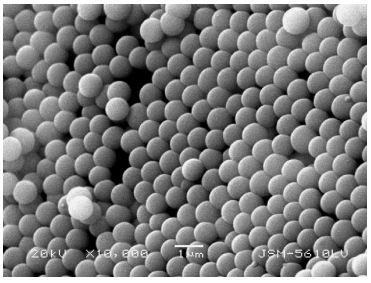

Monodispersed microporous SiO_2 microspheres with high specific surface area were prepared by hydrolysis of tetraethoxysilane (TEOS) using dodecylamine (DDA) as hydrolysis catalyst and the effects of experimental conditions on the morphology and pore parameters of the as-prepared SiO_2 microspheres were investigated and discussed.

Zirconium titanate ceramic pigments: Crystal structure, optical spectroscopy and technological properties
M. Dondi, F. Matteucci and G. Cruciani
Page 233

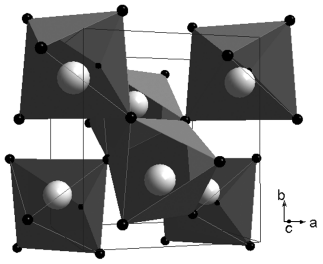

Picture of $ZrTiO_4$ structure.

Synthesis and characteristics of a novel 3-D organic amine oxalate: $(enH_2)_{1.5}[Bi_3(C_2O_4)_6(CO_2CONHCH_2CH_2NH_3)]\cdot 6.5H_2O$
Xiaohong Yu, Hanhui Zhang, Yanning Cao, Yiping Chen and Zhen Wang
Page 247

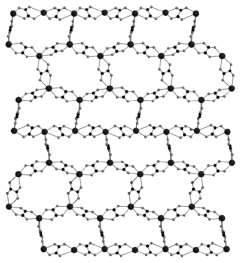

A novel 3-D organic amine oxalate has been synthesized by hydrothermal method. In this compound, the Bi atoms and oxalate units form honeycomb-like layers with two kinds of 6+6 membered aperture. The layers are pillared by oxalate ligands and monamide groups to construct a 3-D framework. At room temperature, the complex exhibits intense blue luminescence with an emission peak at 445 nm.

Influence of metal ions on the structures of Keggin polyoxometalate-based solids: Hydrothermal syntheses, crystal structures and magnetic properties
Zhenyu Shi, Jun Peng, Carlos J. Gómez-García, Samia Benmansour and Xiaojun Gu
Page 253

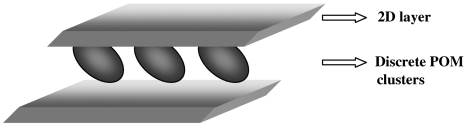

Three new Keggin polyoxometalate-based compounds have been synthesized under hydrothermal condition. These three compounds present the bicapped Keggin anions $[XMo_{12}O_{40}(VO)_2]$ (X=Si, Ge and P) as building blocks. Among the three compounds, compound **3** is a two-dimensional polyoxometalate-based square network formed by bicapped Keggin anions $[PMo_{12}O_{40}(VO)_2]^{4-}$ connected by $[Co(phen)_2]^{2+}$ cations. Discrete bicapped Keggin anions $[PMo_{12}O_{40}(VO)_2]$ linked to two $[Co(phen)_2(OH)]^{+}$ cations are located between the layers.

White-light-emitting long-lasting phosphorescence in Dy^{3+}-doped $SrSiO_3$
Jinyong Kuang, Yingliang Liu and Jianxian Zhang
Page 266

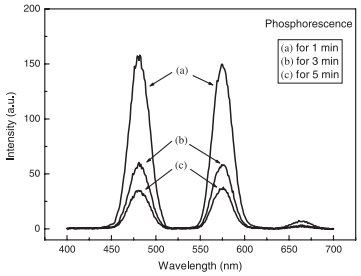

Long-lasting phosphorescence spectra of $SrSiO_3$:Dy^{3+} phosphor at different times (λ_{ex} = 254 nm, a = 1, b = 3, c = 5 min).

Nitrogen-doped zirconia: A comparison with cation stabilized zirconia
Jong-Sook Lee, Martin Lerch and Joachim Maier
Page 270

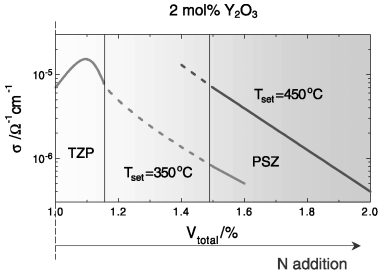

Conductivity profiles in nitrogen-graded zirconia represented as a function of vacancy concentrations using the nitrogen concentration profiles determined by auger electron spectroscopy.

Structural studies on W^{6+} and Nd^{3+} substituted $La_2Mo_2O_9$ materials
David Marrero-López, Jesús Canales-Vázquez, Wuzong Zhou, John T.S. Irvine and Pedro Núñez
Page 278

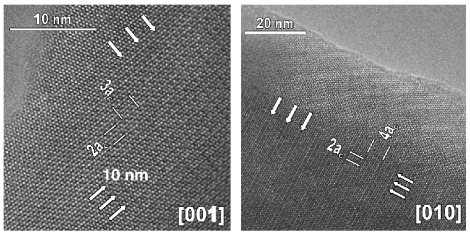

SAED patterns corresponding to the (a) [100], (b) [010] and (c) [001] zone axes, respectively. The patterns could be indexed considering a $2\times3\times4$ superstructure of the β-polymorph with a monoclinic distortion. The diffraction spots are highlighted with large white dots from the β-type basic unit cell and small ones from the $2\times3\times4$ supercell. The unit cell parameter, β, is marked in (b). Bottom: HRTEM images in the [001] and [010] zone axes for the α-$La_2Mo_2O_9$, showing very clearly the $2a_c\times3a_c$ and the $2a_c\times4a_c$ superstructure, respectively.

Continued

Synthesis and crystal structures of $CaY_2Ge_3O_{10}$ and $CaY_2Ge_4O_{12}$
Hisanori Yamane, Ryouji Tanimura, Takahiro Yamada, Junichi Takahashi, Takashi Kajiwara and Masahiko Shimada
Page 289

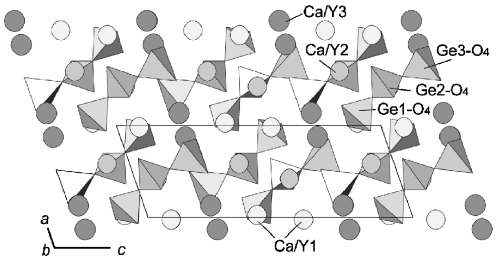

Crystal structure of $CaY_2Ge_3O_{10}$ showing Ge–O_4 tetrahedra (Ge_3O_{10} group).

New mixed-valence chromium structure type: $NH_4Cr(CrO_4)_2$
Barbara M. Casari, Erica Wingstrand and Vratislav Langer
Page 296

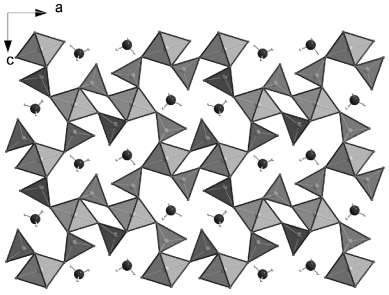

The title compound constitutes a new structure type among the Cr(III)/Cr(VI) ternary oxides, the NH_4-type. The other structure types are forming layers intercalated by the counter ions, while the structure of $NH_4Cr_3O_8$ forms channels containing the ammonium ions.

Solvothermal synthesis and characterisation of new one-dimensional indium and gallium sulphides: $[C_{10}N_4H_{26}]_{0.5}[InS_2]$ and $[C_{10}N_4H_{26}]_{0.5}[GaS_2]$
Paz Vaqueiro
Page 302

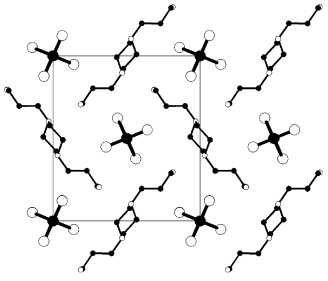

$[C_{10}N_4H_{26}]_{0.5}[InS_2]$ and $[C_{10}N_4H_{26}]_{0.5}[GaS_2]$, prepared under solvothermal conditions, consist of one-dimensional $[MS_2]^-$ chains separated by diprotonated 1,4-bis(3-aminopropyl)piperazine molecules.

Preparation and characterization of $LiNi_{0.8}Co_{0.2}O_2$/PANI microcomposite electrode materials under assisted ultrasonic irradiation
Y. Mosqueda, E. Pérez-Cappe, J. Arana, E. Longo, A. Ries, M. Cilense, P.A.P. Nascente, P. Aranda and E. Ruiz-Hitzky
Page 308

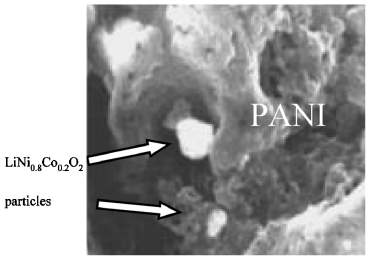

PANI/$LiNi_{0.8}Co_{0.2}O_2$ microcomposites prepared under ultrasound irradiation are formed by oxide particles in contact with the conducting polymer procuring connectivity that enhances electrical and electrochemical properties of the resulting materials.

The reciprocal $CuInS_2 + 2CdSe \Leftrightarrow CuInSe_2 + 2CdS$ system. Part I. The quasi-binary $CuInSe_2$–CdSe system: Phase diagram and crystal structure of solid solutions
I.D. Olekseyuk, O.V. Parasyuk, O.A. Dzham and L.V. Piskach
Page 315

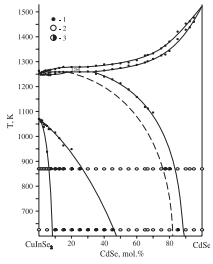

Phase diagram of the $CuInSe_2$–CdSe system (point labels: 1, DTA results; 2, single-phase alloys; 3, two-phase alloys; fields labels: 1, L; 2, L + β; 3, L + γ; 4, α; 5, $\gamma + \alpha$; 6, γ; 7, $\beta + \gamma$; 8, β).

Mechanochemical synthesis and ionic conductivity in the $Gd_2(Sn_{1-y}Zr_y)_2O_7$ ($0 \leqslant y \leqslant 1$) solid solution
K.J. Moreno, A.F. Fuentes, J. García-Barriocanal, C. León and J. Santamaría
Page 323

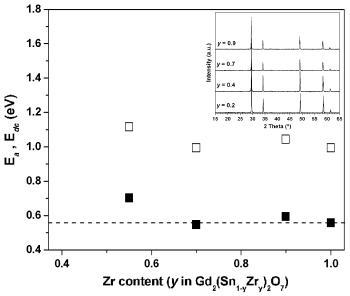

Macroscopic (E_{dc}, empty squares) and microscopic (E_a, solid squares) activation energies for oxygen ion migration as a function of Zr content, for the $Gd_2(Sn_{(1-y)}Zr_y)_2O_7$ solid solution. Inset: DRX patterns of several compositions in the title solid solution with different Sn/Zr ratio.

Rapid Communications

The role of NH_3 atmosphere in preparing nitrogen-doped TiO_2 by mechanochemical reaction

Gang Liu, Feng Li, Zhigang Chen, Gao Qing Lu and Hui-Ming Cheng

Page 331

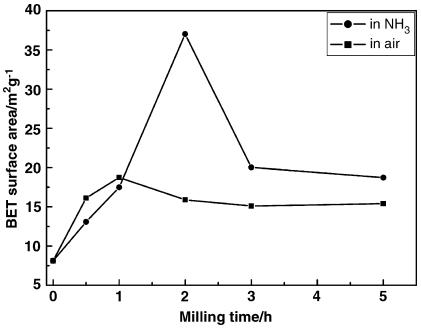

The specific surface area (BET) of titania varies with the increase of milling time in air and gaseous ammonia.

Crystal structure of the pyrochlore oxide superconductor KOs_2O_6

Jun-Ichi Yamaura, Shigeki Yonezawa, Yuji Muraoka and Zenji Hiroi

Page 336

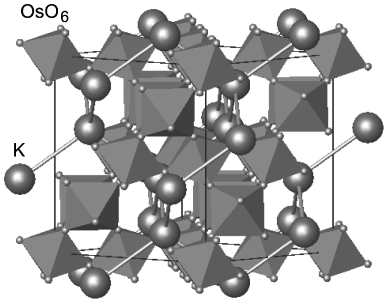

Crystal structure of β-pyrochlore oxide KOs_2O_6. Corner-shared OsO_6 octahedra form a three-dimensional network involving large atomic cage, and a K atom in each cage constitutes a 'hypothetical' diamond lattice.

NOTICE

The Keyword Index for Volume 179 will appear in the December 2006 issue as part of a cumulative index for the year 2006.